Electronic Supplementary Material (ESI) for Materials Horizons.
This journal is © The Royal Society of Chemistry 2021

Supplementary Information

Engineering of flat bands and Dirac bands in two-dimensional covalent organic frameworks (COFs): Relationships among molecular orbital symmetry, lattice symmetry, and electronic-structure characteristics

Xiaojuan Ni,[1] Hong Li,[1] Feng Liu,[2] and Jean-Luc Brédas[1]

[1] Department of Chemistry and Biochemistry

The University of Arizona, Tucson, Arizona 85721-0088, United States

[2] Department of Materials Science and Engineering

University of Utah, Salt Lake City, Utah 84112, United States

The Supplementary Information (SI) contains further details on computational approaches, supporting figures, and discussion.

Table of Contents

1. Computational approaches S3

a. Density functional theory calculations

b. Tight-binding model

2. Kagome bands as a function of the sign of the lattice hopping parameter S11

3. TANG frontier molecular orbitals and partial charge distributions of P^2TANG COF S13

4. TPB frontier molecular orbitals and partial charge distributions of TPB-COF S14

5. Kagome bands in BTA-PDA COF and COF-5 ..... S15

6. Multi-layer BTA-PDA COFs S17

7. Bulk COF electronic bands S18

8. COF binding energies S20

9. Further details on the COFs discussed in the main text S21

References S22

1. Computational approaches

a. Density functional theory calculations

Since our interest here lies on the qualitative features of the 2D COF band structures, the DFT band-structure calculations for the COFs were carried out in the framework of the Perdew-Burke-Ernzerhof generalized gradient approximation functional using the Vienna ab initio simulation package (VASP).[1,2] All the self-consistent calculations were performed with a plane-wave cutoff of 500 eV and a vacuum layer over 15 Å thick to ensure electronic decoupling between neighboring slabs. Monkhorst-Pack *k*-point meshes of 3×3×1 and 3×3×15 used for monolayer and bulk COFs, respectively. Dispersion corrections of the van der Waals interactions (DFT-D2) were considered in the calculations on multi-layer thin films and bulk. In the geometry optimization, all the atoms are allowed to relax until the atomic forces are smaller than 0.01 eV/Å. The MO analysis of the individual core and linker molecules were performed at the B3LYP 6-31G level with the Gaussian16 program.[3] All the geometries of the molecules and 2D COFs were optimized in the ground state.

b. Tight-binding model

The Hamiltonian of a TB model considering a single-orbital hopping or multi-orbital [(π_x, π_y) or (σ, π_x, π_y)] hopping in a lattice can be expressed as:

$$H = \sum_{i\alpha} \varepsilon_{i\alpha} c_{i\alpha}^{\dagger} c_{i\alpha} - \sum_{\langle i\alpha, j\beta \rangle} t c_{i\alpha}^{\dagger} c_{j\beta} + hc, \quad \text{(S1)}$$

where $\varepsilon_{i\alpha}$ is the on-site energy of the α orbital at the *i*-th site; $c_{i\alpha}^{\dagger}$ and $c_{i\alpha}$ denote the electron creation and annihilation operators of the α orbital at the *i*-th site, respectively; $\langle i, j \rangle$ denotes nearest-neighbor hopping with parameter t, which is expressed within the Slater-Koster scheme.[4]

Defining the orbital basis. The cores in hexagonal COFs have three-fold symmetry, which means that their MO levels can be doubly degenerate. For instance, in the case of benzene, the six carbon p_z AOs lead to six π-MOs, as shown in **Figure S1**;[5,6] the frontier MOs turn out to be doubly degenerate (see **Figures S1a** and **S1b**): π_2 and π_3 are the HOMOs; π_4 and π_5 are the LUMOs.

We now illustrate how to generate a more complete and robust orbital basis for TB models by considering the frontier MOs of benzene as an example. The procedure that has been followed in the physics community to derive the orbital basis is to focus on the phase of the wavefunction *above* the molecular plane:

• First, by looking at **Figures S1b and S1d**, the π_2 and π_3 HOMOs can be taken as corresponding to the bonding combination of two *p*-like orbitals located on two adjacent (equivalent) atoms: On the one hand, two p_x-like orbitals forming a "diatomic" π_x-like orbital in the case of π_2, with *x* along the long molecular axis; on the other hand, two p_y-like orbitals forming a "diatomic" π_y orbital in the case of π_3, with *y* along the short molecular axis. In a similar way, the π_4 and π_5 LUMOs can be pictured as the antibonding combination of two adjacent p_x-like and p_y-like orbitals, respectively.

• The next step is to combine the π_2 and π_3 [π_4 and π_5] HOMOs [LUMOs], which we do by simply superposing the wavefunctions of the degenerate levels. This leads to the description shown in **Figure S1c**, which illustrates that the degenerate HOMO [LUMO] levels of benzene can be, in an effective way, represented by a combination of π_x and π_y [π_x^* and π_y^*] orbitals. Also, the π_1- and π_6-MOs of benzene possess six- and three-fold rotational symmetry along the *z* axis; as a whole, they can be approximately treated as σ- and σ*-MOs, respectively.[7,8]

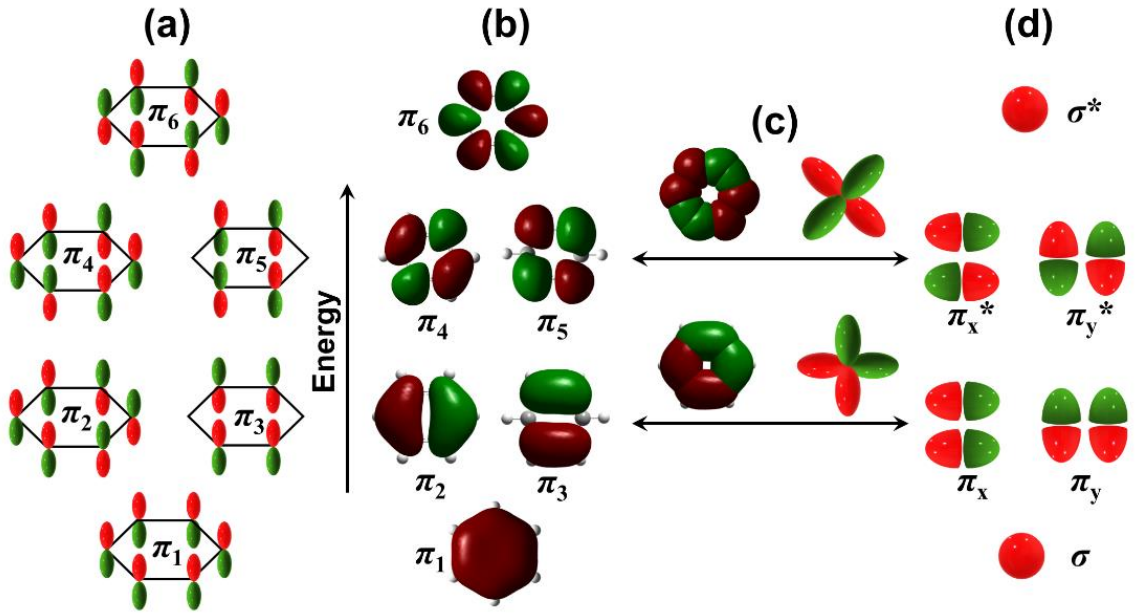

Figure S1. Illustration of the building of the TB orbital basis in benzene from the π-MOs. (a) Description of the π-MOs of benzene as formed from six pz AOs: (**a**) side view and (**b**) top view. (**c**) shows the superposition of the degenerate MO levels and part (**d**) depicts the MOs in the framework of a homogeneous diatomic molecule. Red and green indicate positive and negative phases of the wavefunctions.

Defining the hopping integrals. The effective correspondence we have shown between the actual MOs of benzene and the σ-, π_x-, and π_y-MOs derived from a diatomic-molecule picture is the key to exploit the so-called Slater-Koster scheme[4] and define the hopping terms in the TB model, see **Figure S2**. For the sake of avoiding confusion with the atomic orbital terminology (s, p_x, and p_y) generally chosen in the physics community, in the following discussion, we will use σ, π_x, and π_y notations described above to represent the MOs.

The hopping between two σ orbitals is the simplest case and the corresponding integral is denoted as ssσ (see **Figure S2a**).

• When considering π_x and/or π_y orbitals, we need to account for the angular dependence of the hopping integrals and consider a new system of coordinates. For instance, the π_x orbital in the case of σ-π_x hopping can be decomposed into two components along the *x* ($cos\varphi$) and *y* ($sin\varphi$) axes in new coordinates defined by rotating the initial coordinate system counterclockwise with an angle φ until the *x* axis is parallel to the vector connecting the two orbitals. The integral for the component perpendicular to *x* is zero by symmetry, leading to the overall σ-π_x hopping integral being sp$\sigma*cos\varphi$ (where * denotes a product), as shown in **Figure S2b**. Similarly, the σ-π_y hopping integral is derived as sp$\sigma*sin\varphi$ (see **Figure S2c**).

• The same approach also works for π-orbital combinations. In the case of π_x-π_x hopping, each π_x can be decomposed into two components, parallel and perpendicular to the *x* axis in the new coordinates. The hopping integral becomes a sum of two terms: [pp$\sigma*cos^2\varphi$]+[pp$\pi*sin^2\varphi$] (see **Figure S2d**); note that the other two terms involving $sin\varphi*cos\varphi$ are zero by symmetry. In like manner, the π_y-π_y hopping integral is expressed as [pp$\sigma*sin^2\varphi$]+[pp$\pi*cos^2\varphi$] (see **Figure S2e**). The π_x-π_y case can be derived to give a hopping integral equal to [pp$\sigma*sin\varphi*cos\varphi$]–[pp$\pi*sin\varphi*cos\varphi$]; note that, here, owing to the opposite phases of the wavefunctions when decomposing two π orbitals perpendicular to *x*, the sign of the ppπ integral needs to be switched (see **Figure S2f**).

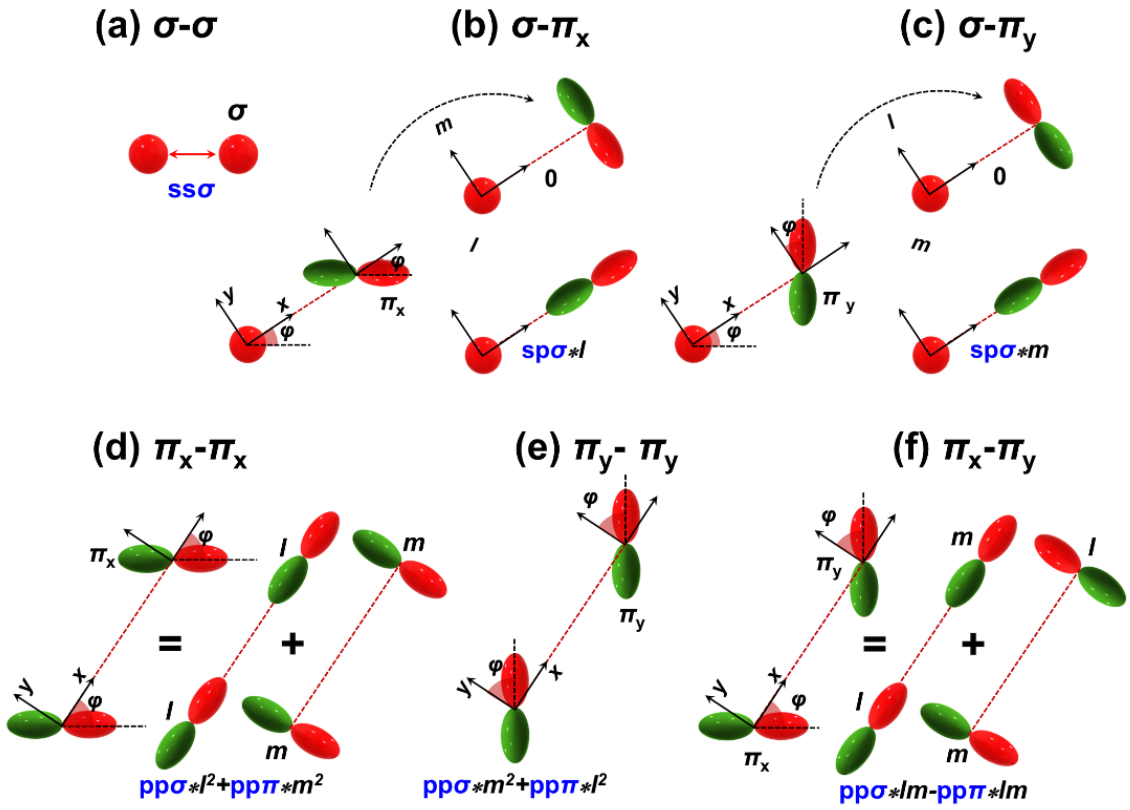

Figure S2. Illustrations of the TB hopping integrals following the Slater-Koster scheme between two orbitals: (**a**) σ and σ, (**b**) σ and π_x, (**c**) σ and π_y, (**d**) π_x and π_x, (**e**) π_y and π_y, and (**f**) π_x and π_y. The ssσ, spσ, ppσ, and ppπ hopping integral parameters are highlighted in blue, with $l = cos\varphi$ and $m = sin\varphi$. Red and green indicate positive and negative phases of the wavefunctions.

The momentum space (*k*-space) Hamiltonian can be obtained by transforming Eq. (S1) into *k*-space. The illustration of single-orbital hopping in a honeycomb lattice is shown in **Figure 2a**. Its *k*-space Hamiltonian writes:

$$H(\vec{k}) = \begin{pmatrix} \varepsilon_0 & -t\left(e^{ik_1} + e^{ik_2} + e^{ik_3}\right) \\ -t\left(e^{-ik_1} + e^{-ik_2} + e^{-ik_3}\right) & \varepsilon_0 \end{pmatrix}, \text{(S2)}$$

where k_n is defined as $k_n = \vec{k} \cdot \overrightarrow{a_n}$ with three NN hopping vectors $\overrightarrow{a_1} = \left(-\frac{\sqrt{3}}{2}\hat{x} - \frac{1}{2}\hat{y}\right)$, $\overrightarrow{a_2} = \hat{y}$, and $\overrightarrow{a_3} = \left(\frac{\sqrt{3}}{2}\hat{x} - \frac{1}{2}\hat{y}\right)$.

The general form of the *k*-space Hamiltonian of a TB model considering multi-orbital hopping on each lattice site, such as the H-XY model and H-SP2 model, is $H(\vec{k}) = \begin{pmatrix} \varepsilon & H_0 \\ H_0^* & \varepsilon \end{pmatrix}$. For the H-XY model, as illustrated in **Figures 3b** and **3c**, the matrix elements ε and H_0 are $\varepsilon = \begin{pmatrix} \varepsilon_\pi & 0 \\ 0 & \varepsilon_\pi \end{pmatrix}$ and

$$H_0 = \begin{pmatrix} \frac{1}{4}(3\mathrm{pp}\sigma + \mathrm{pp}\pi)(e^{ik_1} + e^{ik_3}) + \mathrm{pp}\pi e^{ik_2} & \frac{\sqrt{3}}{4}(\mathrm{pp}\sigma - \mathrm{pp}\pi)(e^{ik_1} - e^{ik_3}) \\ \frac{\sqrt{3}}{4}(\mathrm{pp}\sigma - \mathrm{pp}\pi)(e^{ik_1} - e^{ik_3}) & \frac{1}{4}(\mathrm{pp}\sigma + 3\mathrm{pp}\pi)(e^{ik_1} + e^{ik_3}) + \mathrm{pp}\sigma e^{ik_2} \end{pmatrix}. \text{(S3)}$$

For the H-SP2 model, as illustrated in **Figure 4a**, the corresponding ε and H_0 are expressed as $\varepsilon = \begin{pmatrix} \varepsilon_\sigma & 0 & 0 \\ 0 & \varepsilon_\pi & 0 \\ 0 & 0 & \varepsilon_\pi \end{pmatrix}$

and $H_0 = \begin{pmatrix} \mathrm{ss}\sigma(e^{ik_1} + e^{ik_2} + e^{ik_3}) & -\frac{\sqrt{3}}{2}\mathrm{sp}\sigma(e^{ik_1} - e^{ik_3}) & -\frac{1}{2}\mathrm{sp}\sigma(e^{ik_1} - 2e^{ik_2} + e^{ik_3}) \\ \frac{\sqrt{3}}{2}\mathrm{sp}\sigma(e^{ik_1} - e^{ik_3}) & \frac{1}{4}(3\mathrm{pp}\sigma + \mathrm{pp}\pi)(e^{ik_1} + e^{ik_3}) + \mathrm{pp}\pi e^{ik_2} & \frac{\sqrt{3}}{4}(\mathrm{pp}\sigma - \mathrm{pp}\pi)(e^{ik_1} - e^{ik_3}) \\ \frac{1}{2}\mathrm{sp}\sigma(e^{ik_1} - 2e^{ik_2} + e^{ik_3}) & \frac{\sqrt{3}}{4}(\mathrm{pp}\sigma - \mathrm{pp}\pi)(e^{ik_1} - e^{ik_3}) & \frac{1}{4}(\mathrm{pp}\sigma + 3\mathrm{pp}\pi)(e^{ik_1} + e^{ik_3}) + \mathrm{pp}\sigma e^{ik_2} \end{pmatrix}$. (S4)

Due to the complexity of the H-SP2 model, it can lead to different types of band structure depending on the relative magnitude of its parameters.

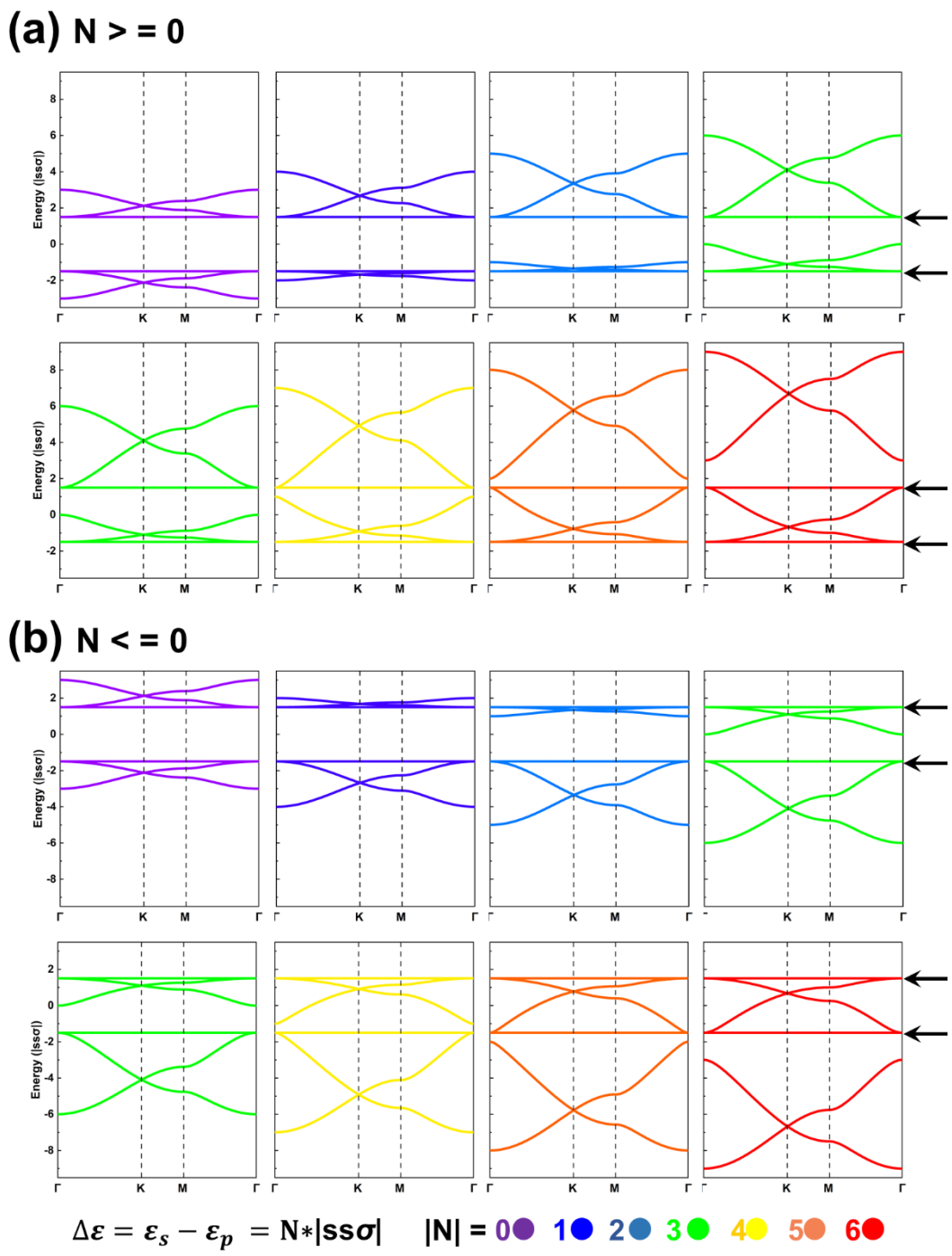

Figure S3. Band structures obtained from the H-SP2 models with ε_π = 0, spσ = -ssσ, ppσ = -ssσ, and ppπ = 0. $\Delta\varepsilon$ is defined as the energy difference between ε_σ and ε_π: $\Delta\varepsilon$ = N*|ssσ|. (**a**) N = 0, 1, 2, 3 4, 5, and 6. (**b**) N = 0, -1, -2, -3, -4, -5, and -6. The black arrows indicate the positions of the flat bands.

Figure S3 shows the band structures obtained from the H-SP2 model when all the hopping integrals except ppπ are of comparable magnitudes, *i.e.*, |ssσ| = |spσ| = |ppσ|. The positions of the two flat bands remain unchanged with respect to the *s*-orbital on-site energy, as indicated by the black arrows in **Figure S3**. The limiting conditions of having $\varepsilon_\sigma = 0$ and $\varepsilon_\pi = 0$ ($\Delta\varepsilon = \varepsilon_\sigma - \varepsilon_\pi = 0$) are taken as the starting point, see the purple bands in **Figure S3**. Two sets of kagome bands are obtained and separated by two flat bands. When ε_σ is slightly higher than ε_π ($\Delta\varepsilon = |ss\sigma|$, see the blue bands in **Figure S3a**), there still appear two sets of kagome bands with two flat bands close to each other. However, the realization of such band dispersion ($\Delta\varepsilon = |ss\sigma|$) remains elusive in COFs since $\Delta\varepsilon$ is usually much larger than the hopping integrals. Upon further increase of the energy difference $\Delta\varepsilon$, there appear two sets of parallel kagome bands with the flat band at the bottom [see the cyan ($\Delta\varepsilon = 2|ss\sigma|$), green ($\Delta\varepsilon = 3|ss\sigma|$), and yellow ($\Delta\varepsilon = 4|ss\sigma|$) bands in **Figure S3a**. Furthermore, after considering a larger $\Delta\varepsilon$, the middle flat band touches the bottom kagome bands to form the four bands typical of a H-XY model; the two Dirac bands on the top arise predominantly from *s*-orbital hopping in a hexagonal lattice [see the orange ($\Delta\varepsilon = 5|ss\sigma|$) and red ($\Delta\varepsilon = 6|ss\sigma|$) bands in **Figure S3a**]. On the other hand, when ε_σ is lower than ε_π, as shown in **Figure S3b**, the band dispersions are upside-down compared to those corresponding to $\Delta\varepsilon > 0$ in **Figure S3a**. It is clear that a significant on-site energy difference between σ and π orbitals separates the six bands into two groups dominated by the σ orbital (two Dirac bands) and the π orbitals (the four bands typical of a H-XY model), respectively.

The TB model considering single-orbital hopping in a kagome lattice is illustrated in **Figure 5a**. Its *k*-space Hamiltonian is $H(\vec{k}) = \begin{pmatrix} \varepsilon_0 & -2t\cos k_3 & -2t\cos k_2 \\ -2t\cos k_3 & \varepsilon_0 & -2t\cos k_1 \\ -2t\cos k_2 & -2t\cos k_1 & \varepsilon_0 \end{pmatrix}$. (S5)

2. Kagome bands as a function of the sign of the lattice hopping parameter

For single-orbital hopping in a kagome lattice, there is one flat band located either above or below two Dirac bands depending on the sign of the lattice hopping parameter, as illustrated in **Figure S4**. There are three sites located around the shaded triangle in the kagome lattice unit cell. Starting with the **a1** case, the orbitals on neighboring sites have (say) positive-phase lobes facing each other and all positive hopping integrals. By switching the phase sign on one site (as indicated by the yellow dot in part **a2**), one obtains a hopping pattern with one positive hopping parameter and two negative hopping parameters, as shown in part **a2** in **Figure S4a**. The same hopping pattern as for **a2** can be achieved by switching the phase sign on a second site, as indicated by the yellow dot in part **a3**. The last scenario is to switch the phase sign of the third site (as indicated by the yellow dot in part **a4**); all hopping parameters are then positive, which is equivalent to part **a1**. These four hopping patterns, for which there is always zero or an even number of negative *t* values, lead to the flat band being on the top of kagome bands, as shown in **Figure S4b**.

On the contrary, when all the orbitals on neighboring sites have the phases of the lobes facing each other alternating (see part **c1** in **Figure S4c**), the hopping parameters are all negative. Then, playing the same game as before, that is by switching sequentially the phase of the sites one by one, as indicated by the yellow dots in **Figure S4c**, we find that there is always an odd number of negative hopping parameters. The hopping patterns in **Figure S4c** all lead to the kagome bands with the flat band at the bottom, see **Figure S4d**. Therefore, in order to determine the location of the flat bands in a set of kagome bands, it is necessary to perform the MO analysis on a COF fragment instead of an isolated molecule representing the linker unit.

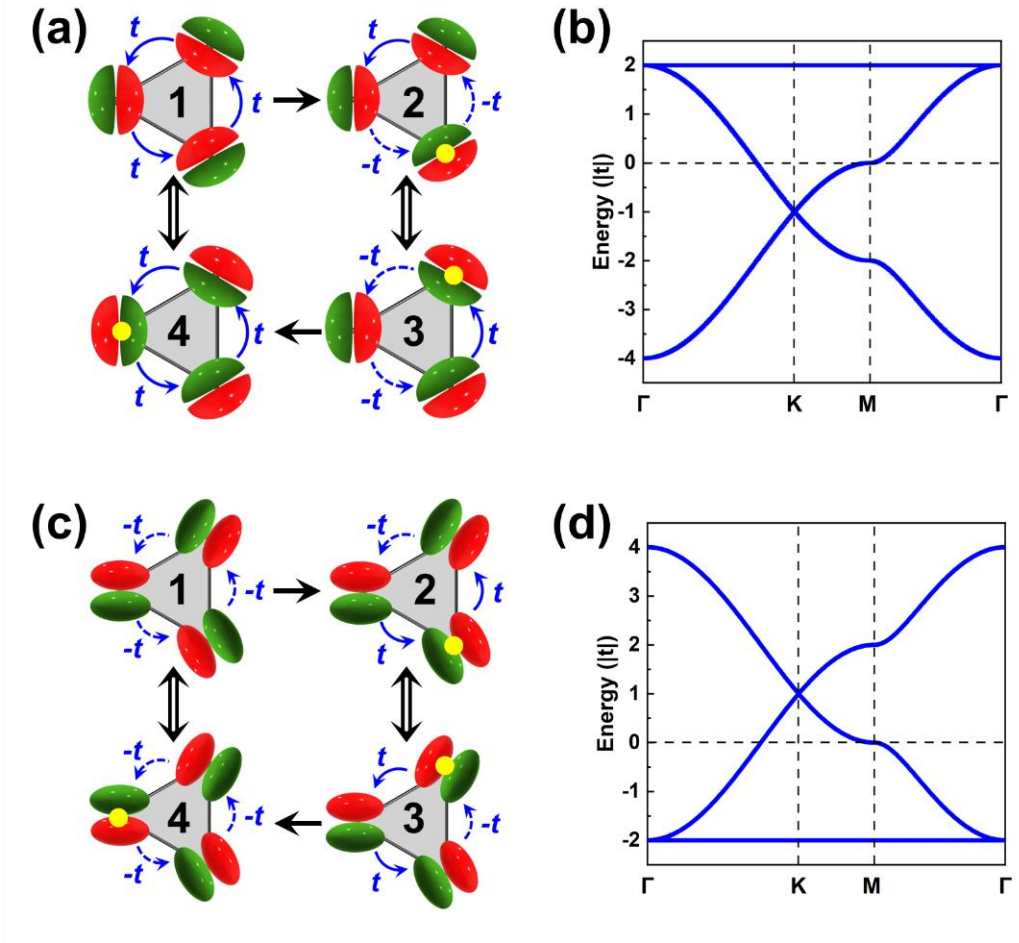

Figure S4. Illustration of the flat band location in kagome bands as a function of the sign of the lattice hopping parameter in a three-atom (shaded triangle) kagome-lattice unit cell. (**a**) Typical patterns of hopping between neighboring sites lead to (**b**) the kagome bands with flat band on the top. (**c**) Typical patterns of hopping between neighboring sites lead to (**d**) the kagome bands with flat band on the bottom. Red and green indicate the positive and negative phase of lobes. *t* represents the nearest neighbor hopping, as indicated by the solid arrow. The negative sign indicates the hopping between two orbitals with opposite signs of lobes facing each other, labeled as dashed arrow.

3. TANG frontier molecular orbitals and partial charge distributions of P^{2}TANG COF

As shown in **Figure S5a**, TANG has a doubly degenerate LUMO level, which is energetically well separated from the LUMO+1 level. The HOMO corresponds to a single level, well-separated from the doubly degenerate HOMO-1 level. The DFT-calculated partial charge distribution corresponding to the CBs confirms the major contribution from the TANG LUMO, which can be seen by the correspondence between the superposition of the LUMO and the CB partial charge distributions illustrated in the top panel of **Figure S5b**. The partial charge distribution of top two Dirac VBs (VB1) correlates with the TANG HOMO; also, the wavefunction superposition of the degenerate HOMO-1 level has the same spatial distribution as the VB2 partial charge distribution.

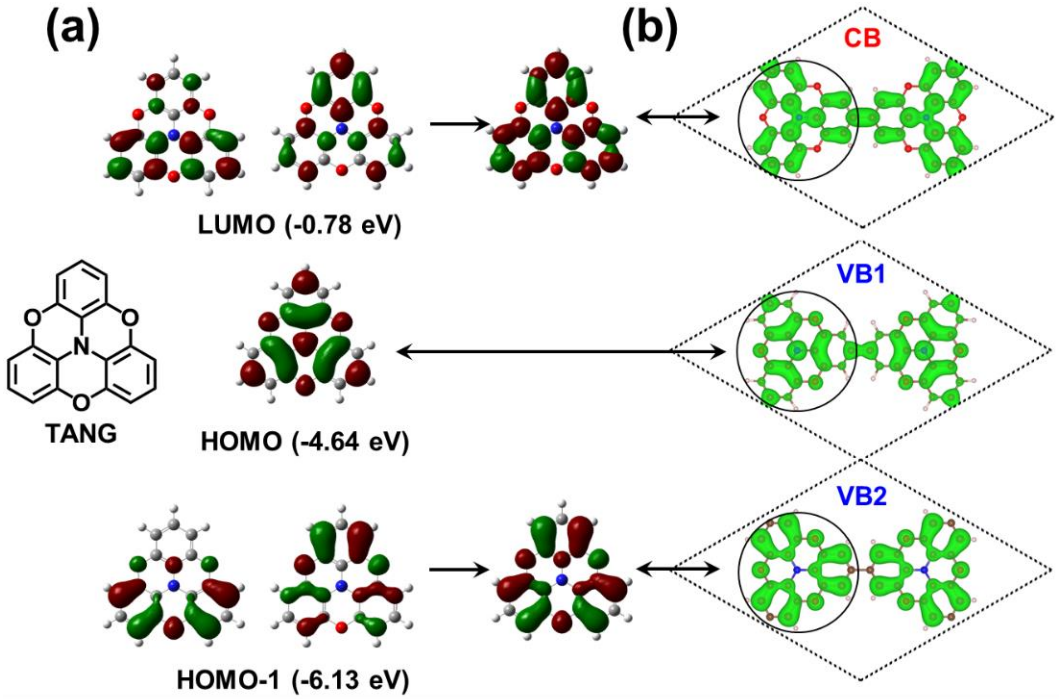

Figure S5. (**a**) DFT-calculated frontier MOs of the isolated TANG molecule. (**b**) DFT partial charge distributions of P^{2}TANG COF in the CBs and VBs. The dashed rhombus indicates the unit cell.

4. TPB frontier molecular orbitals and partial charge distributions of TPB-COF

The TPB frontier MOs are shown in **Figure S6a**. The TPB LUMO is doubly degenerate and can serve as the orbital basis for an H-XY model or, with the additional consideration of the LUMO+1 level, for an H-SP2 model. The same analysis can be applied to the degenerate HOMO level and the HOMO-1 level, following either a H-XY or a H-SP2 model. The partial charge distributions related to the CBs and VBs of the TPB COF are shown in **Figure S6b** and correlate very well with the combination of the TPB MOs we have considered.

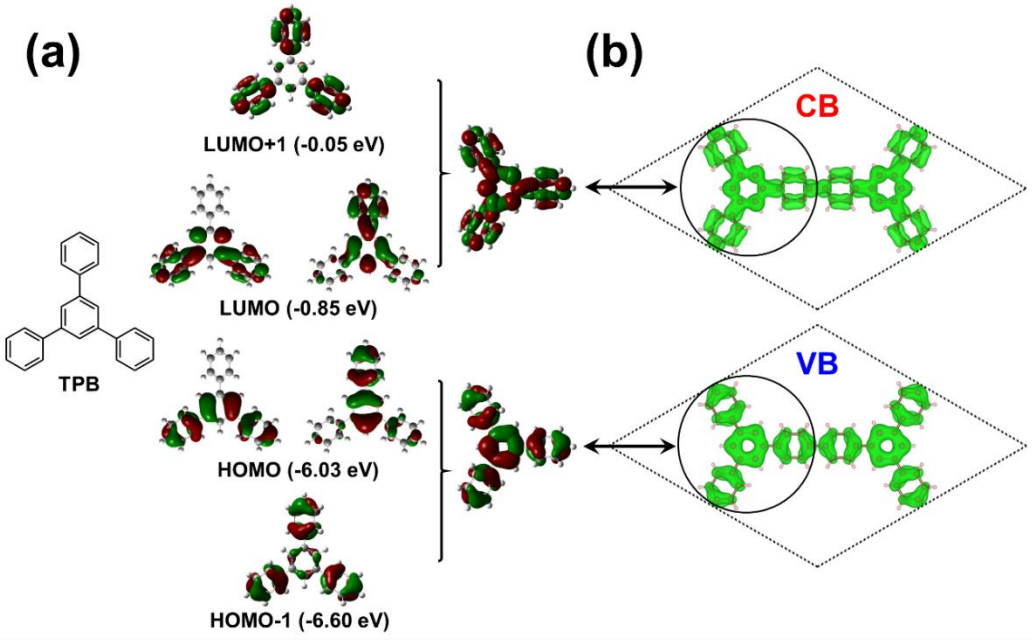

Figure S6. (**a**) DFT-calculated frontier MOs of the isolated TPB molecule. (**b**) DFT partial charge distributions of TPB-COF in the CBs and VBs. The dashed rhombus indicates the unit cell.

5. Kagome bands in BTA-PDA COF and COF-5

The COF fragments containing of one core unit and three linker units for the BTA-PDA COF and COF-5, as shown in **Figures S7a** and **S7c**, were adopted to perform the MO analysis, respectively. In the case of BTA-PDA COF (see **Figure 9**), the top VBs have predominant contributions from the PDA HOMO. The superposition of three frontier occupied MOs (see **Figure S7b)** in the COF fragment indicate the lattice hopping sign between neighboring kagome-site linker units follows the scheme illustrated in **Figure S4a**. As a result, the kagome VBs of the BTA-PDA COF have the flat band located on the top. Similarly, the superposition of three frontier unoccupied MOs of a COF-5 fragment (see **Figure S7d**) elucidates the sign of the lattice hopping parameters between neighboring kagome-site linker units, following the scheme illustrated in **Figure S4a** and giving the flat band on the top among the kagome CBs in COF-5 (see **Figure 10**).

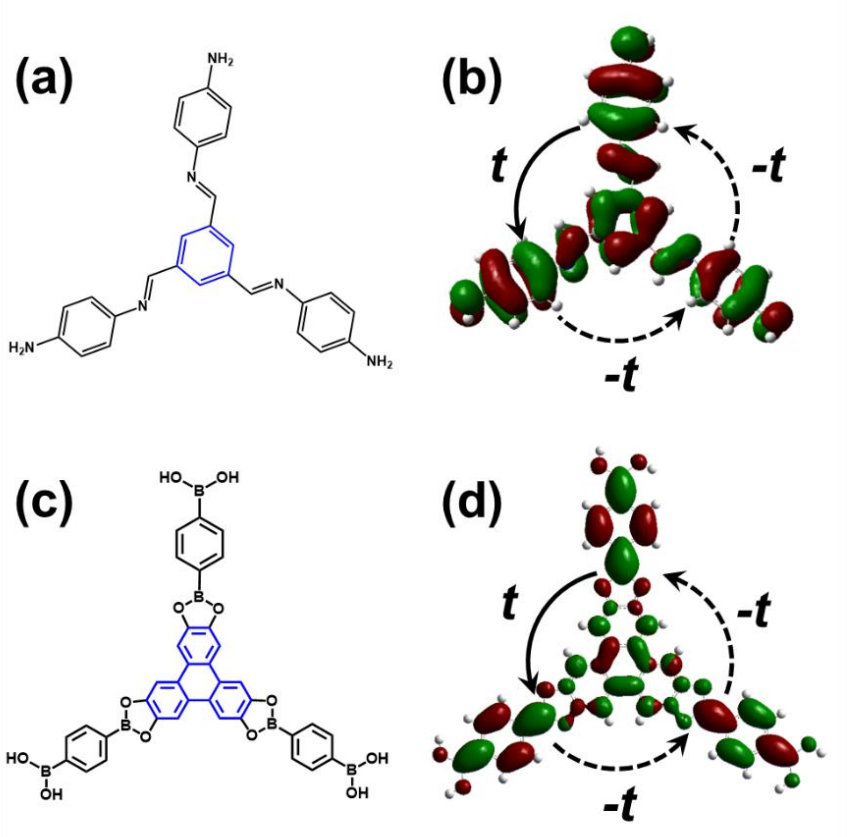

Figure S7. The structures of COF fragment containing one core unit and three linker units: (**a**) the BTA-PDA COF and (**c**) COF-5. The superposition of (**b**) three frontier occupied MOs contributed to the kagome VBs in the BTA-PDA COF and (**d**) three frontier unoccupied MOs contributed to the kagome CBs in COF-5, respectively. The positive and negative lattice hopping parameters are labeled as solid and dashed arrows, respectively.

6. Multi-layer BTA-PDA COFs

Taking the BTA-PDA COF as an example, we calculated the band structures of bilayer and trilayer COFs, as shown in **Figures S8a** and **S8c**. The bilayer and trilayer COFs have the same features of band dispersion as those of monolayer but with a reduced band gap (1.49 and 1.26 eV respectively, *vs.* 2.05 eV for the monolayer) due to interlayer coupling. The partial charge distributions in the conduction bands and valence bands for bilayer and trilayer BTA-PDA COFs are shown in **Figures S8b** and **S8d**.

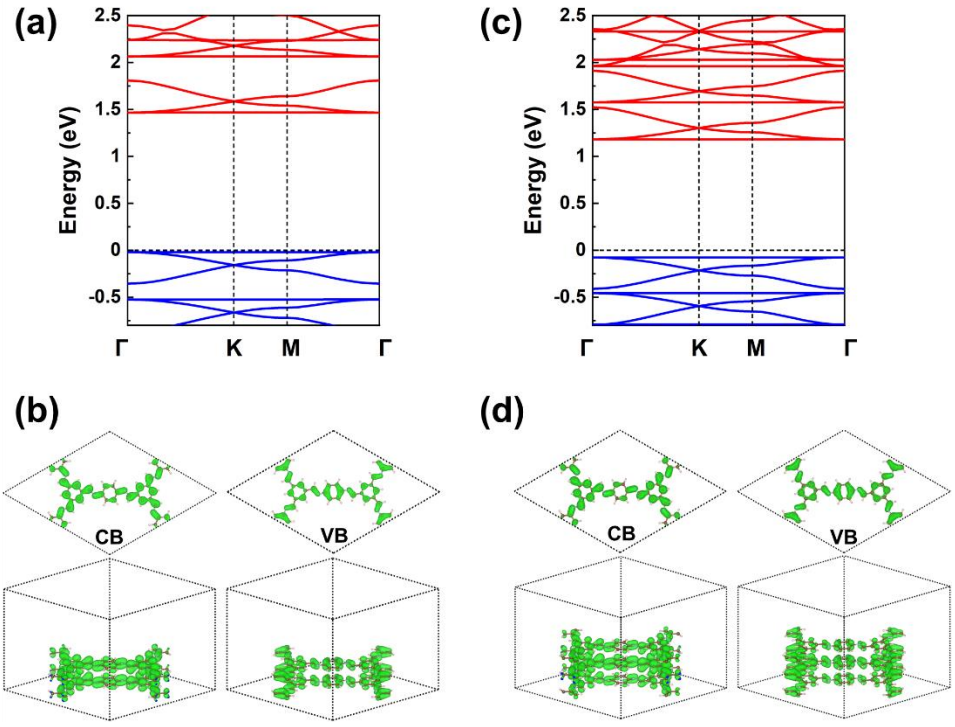

Figure S8. DFT band structures of (**a**) bilayer and (**c**) trilayer BTA-PDA COFs. Partial charge distributions in the CBs and VBs for (**b**) bilayer and (**d**) trilayer BTA-PDA COFs. The VBs and CBs are colored in blue and red, respectively.

7. Bulk COF electronic bands

We have calculated the electronic bands of three representative bulk COFs, as shown in **Figure S9**. The bulk COF structures with AA-type stacking (see **Figures S9a**, **S9c**, and **S9e**) are fully geometry relaxed. The in-plane lattice constant of the bulk TPB COF (space group: P622, No. 177), BTA-PDA COF (space group: P6/m, No. 175), and COF-5 (space group: P6/mmm, No. 191) are calculated to be 22.42, 22.45, and 30.14 Å, respectively. The interlayer distances are 3.62, 3.56, and 3.57 Å, respectively. **Figures S9b**, **S9d**, and **S9f** show the band structures. Note that the direct band gaps of the TPB COF and the BTA-PDA COF remain nearly unchanged over the first Brillouin zone; in other words, the interlayer (Γ to A) dispersions of the top VB and bottom CB are very much alike, as seen from **Figures S9b** and **S9d**. In contrast, in COF-5, the bottom CB dispersion is substantially larger than the top VB dispersion, making the direct gap smaller at point *A*. The CBs and VBs near the Fermi level of bulk COFs maintain the salient features of those in the COF monolayer but with a reduced band gap owing to the interlayer coupling, indicating that the correspondence between the frontier MOs of the core and linker units and the electronic bands remains valid for the bulk COFs.

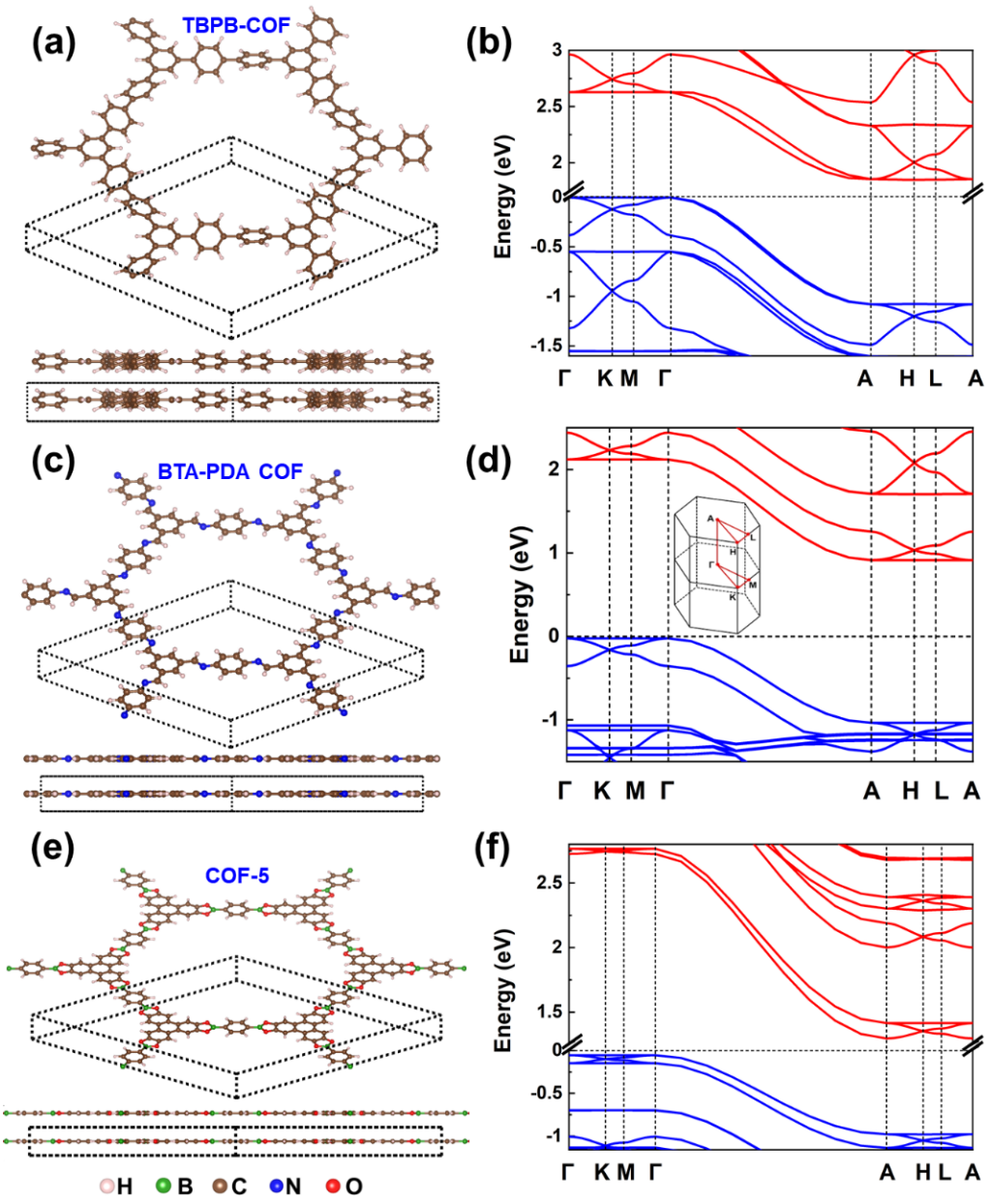

Figure S9. Top view and side view of bulk COFs: (**a**) the TPB COF, (**c**) the BTA-PDA COF, and (**e**) COF-5. The dashed box indicates the unit cell. DFT band structures of bulk COFs: (**b**) TPB COF, (**d**) BTA-PDA COF, and (**f**) COF-5. The inset in (**d**) indicates the first Brillouin zone of the bulk hexagonal COFs. The VBs and CBs are colored in blue and red, respectively.

8. COF binding energies

The interlayer binding energies of the BTA-PDA COF and COF-5 have been calculated as a function of interlayer distance, *d*, with AA-type stacking, as illustrated in **Figures S10a** and **S10c**. The binding energy, E_B, is calculated to be ~14 meV/atom (~0.323 kcal/mol per atom) for the BTA-PDA COF [**Figure S10b**] and ~18 meV/atom (~0.415 kcal/mol per atom) for COF-5 [**Figure S10d**], respectively. These values of E_B fall into the typical range of van der Waals interlayer strength, [9–14] such as that in graphite (~20 meV/atom, ~0.461 kcal/mol per atom).[9,11,12] This points to the feasibility of exfoliating bulk BTA-PDA COF and COF-5 into 2D monolayers.

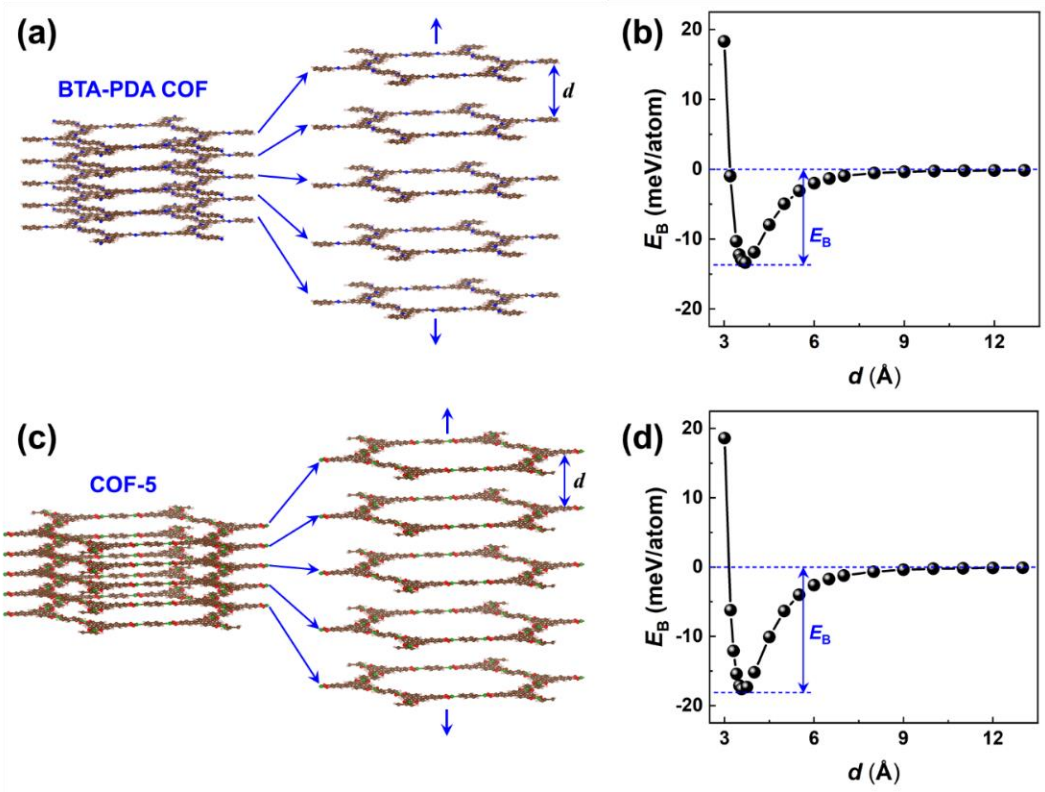

Figure S10. Illustrations of (**a**) BTA-PDA COF and **(c**) COF-5 structures with increasing interlayer distance, *d*. Energy as a function of interlayer distance for (**b**) BTA-PDA COF and (**d**) COF-5, from which the interlayer binding energy, E_B, can be derived.

9. Further details on the COFs discussed in the main text

P^{2}TANG COF. This COF (see **Figure 1a**) has been synthesized via Ullmann coupling of the tribromotrioxaazatriangulene (TBTANG) precursors.[15] The DFT-optimized lattice constant is 17.12 Å, which is consistent with the measured value of ~17.3 Å[15] as well as the previously calculated value of 17.07 Å.[16]

TPB COF. TBPB (*i.e.*, 1,3,5-tris(4-bromophenyl)benzene) has served as the precursor to synthesize the 1,3,5-triphenylbenzene (TPB) COF (see **Figure 1b**) on graphite and metal substrates.[17–19] The lattice constant of a monolayer TPB COF is calculated to be 22.51 Å, which is comparable to the experimental value of 22 Å.[17]

BTA-PDA COF. This COF has been synthesized via the condensation of benzene-1,3,5-tricarbaldehyde (BTA) with *p*-phenylene-diamine (PDA),[20–23] see **Figure 1c**. The lattice constant of a BTA-PDA COF monolayer is 22.51 Å, comparable to the experimental value of 21±1.0 Å.[20]

COF-5. The lattice constant of a COF-5 monolayer (see **Figure 1d**) is calculated to be 30.22 Å, which is close to the measured value of ~30 Å and the previously calculated value of 30.2 Å.[24–29]

References

1 G. Kresse and J. Furthmuller, *Phys. Rev. B*, 1996, **54**, 11169–11186.

2 J. P. Perdew, K. Burke and M. Ernzerhof, *Phys. Rev. Lett.*, 1997, **78**, 1396–1396.

3 M. J. Frisch, G. W. Trucks, H. B. Schlegel, G. E. Scuseria, M. A. Robb, J. R. Cheeseman, G. Scalmani, V. Barone, G. A. Petersson, H. Nakatsuji, X. Li, M. Caricato, A. V Marenich, J. Bloino, B. G. Janesko, R. Gomperts, B. Mennucci, H. P. Hratchian, J. V Ortiz, A. F. Izmaylov, J. L. Sonnenberg, D. Williams-Young, F. Ding, F. Lipparini, F. Egidi, J. Goings, B. Peng, A. Petrone, T. Henderson, D. Ranasinghe, V. G. Zakrzewski, J. Gao, N. Rega, G. Zheng, W. Liang, M. Hada, M. Ehara, K. Toyota, R. Fukuda, J. Hasegawa, M. Ishida, T. Nakajima, Y. Honda, O. Kitao, H. Nakai, T. Vreven, K. Throssell, J. A. Montgomery Jr., J. E. Peralta, F. Ogliaro, M. J. Bearpark, J. J. Heyd, E. N. Brothers, K. N. Kudin, V. N. Staroverov, T. A. Keith, R. Kobayashi, J. Normand, K. Raghavachari, A. P. Rendell, J. C. Burant, S. S. Iyengar, J. Tomasi, M. Cossi, J. M. Millam, M. Klene, C. Adamo, R. Cammi, J. W. Ochterski, R. L. Martin, K. Morokuma, O. Farkas, J. B. Foresman and D. J. Fox, 2016.

4 J. C. Slater and G. F. Koster, *Phys. Rev.*, 1954, **94**, 1498–1524.

5 J. W. Moskowitz and M. P. Barnet, *J. Chem. Phys.*, 1963, **39**, 1557–1560.

6 J. M. Schulman and J. W. Moskowitz, *J. Chem. Phys.*, 1965, **43**, 3287–3290.

7 R. Griffin and T. Van Voorhis, *MIT Course, 5.61 Phys. Chem.*, 2007.

8 LibreTexts, *Chem.libretexts.org*, 2019.

9 L. A. Girifalco and M. Hodak, *Phys. Rev. B - Condens. Matter Mater. Phys.*, 2002, **65**, 125404.

10 M. O. Sinnokrot, E. F. Valeev and C. D. Sherrill, *J. Am. Chem. Soc.*, 2002, **124**, 10887–10893.

11 T. Björkman, A. Gulans, A. V. Krasheninnikov and R. M. Nieminen, *Phys. Rev. Lett.*, 2012, **108**, 235502.

12 N. Mounet, M. Gibertini, P. Schwaller, D. Campi, A. Merkys, A. Marrazzo, T. Sohier, I. E. Castelli, A. Cepellotti, G. Pizzi and N. Marzari, *Nat. Nanotechnol.*, 2018, **13**, 246–252.

13 S. Wang, A. D. Chavez, S. Thomas, H. Li, N. C. Flanders, C. Sun, M. J. Strauss, L. X. Chen, A. J. Markvoort, J. L. Bredas and W. R. Dichtel, *Chem. Mater.*, 2019, **31**, 7104–7111.

14 R. Zacharia, H. Ulbricht and T. Hertel, *Phys. Rev. B - Condens. Matter Mater. Phys.*, 2004, **69**, 155406.

15 G. Galeotti, F. De Marchi, E. Hamzehpoor, O. MacLean, M. Rajeswara Rao, Y. Chen, L. V. Besteiro, D. Dettmann, L. Ferrari, F. Frezza, P. M. Sheverdyaeva, R. Liu, A. K. Kundu, P. Moras, M. Ebrahimi, M. C. Gallagher, F. Rosei, D. F. Perepichka and G. Contini, *Nat. Mater.*, 2020, **19**, 874–880.

16 Y. Jing and T. Heine, *J. Am. Chem. Soc.*, 2019, **141**, 743–747.

17 R. Gutzler, H. Walch, G. Eder, S. Kloft, W. M. Heckl and M. Lackinger, *Chem. Commun.*, 2009, 4456–4458.

18 M. O. Blunt, J. C. Russell, N. R. Champness and P. H. Beton, *Chem. Commun.*, 2010, **46**, 7157–7159.

19 M. Lackinger, *Chem. Commun.*, 2017, **53**, 7872–7885.

20 L. Xu, X. Zhou, W. Q. Tian, T. Gao, Y. F. Zhang, S. Lei and Z. F. Liu, *Angew. Chemie - Int. Ed.*, 2014, **53**, 9564–9568.

21 L. Xu, Y. Yu, J. Lin, X. Zhou, W. Q. Tian, D. Nieckarz, P. Szabelski and S. Lei, *Nanoscale*, 2016, **8**, 8568–8574.

22 J. Sun, X. Zhou and S. Lei, *Chem. Commun.*, 2016, **52**, 8691–8694.

23 J. Liu, F. Yang, L. Cao, B. Li, K. Yuan, S. Lei and W. Hu, *Adv. Mater.*, 2019, **31**, 1902264.

24 A. P. Côté, A. I. Benin, N. W. Ockwig, M. Keeffe, A. J. Matzger and O. M. Yaghi, *Science*, 2005, **310**, 1166–1170.

25 J. W. Colson, A. R. Woll, A. Mukherjee, M. P. Levendorf, E. L. Spitler, V. B. Shields, M. G. Spencer, J. Park and W. R. Dichtel, *Science*, 2011, **332**, 228–231.

26 X. Liu, J. Tan, A. Wang, X. Zhang and M. Zhao, *Phys. Chem. Chem. Phys.*, 2014, **16**, 23286–23291.

27 J. Niu, L. Li, Y. Wang, J. Su, J. Li and X. Wang, *Science*, 2018, **52**, 48–52.

28 H. Li, A. D. Chavez, H. Li, H. Li, W. R. Dichtel and J.-L. Bredas, *J. Am. Chem. Soc.*, 2017, **139**, 16310–16318.

29 A. Kuc, M. A. Springer, K. Batra, R. Juarez-Mosqueda, C. Wöll and T. Heine, *Adv. Funct. Mater.*, 2020, **30**, 1908004.